Title

Single-cell profiling of prurigo nodularis demonstrates immune-stromal crosstalk driving profibrotic responses and reversal with nemolizumab.

Journal

Journal of Allergy and Clinical Immunology, 153(1)

Authors

Ma, Feiyang

Gharaee-Kermani, Mehrnaz

Tsoi, Lam

et al.

Publication Date

2024

DOI

10.1016/j.jaci.2023.07.005

Peer reviewed

Published in final edited form as:

J Allergy Clin Immunol. 2024 January ; 153(1): 146–160. doi:10.1016/j.jaci.2023.07.005.

Single-cell Profiling of Prurigo Nodularis Demonstrates Prominent Immune-Stromal Crosstalk Driving Profibrotic Responses in COL11A1+ Fibroblasts and Reversal with Nemolizumab

Feiyang Ma, PhD[1], **Mehrnaz Gharaee-Kermani, PhD**[1], **Lam C. Tsoi, PhD**[1,2,3], **Olesya Plazyo, PhD**[1], **Prasad Chaskar, PhD**[4], **Paul Harms, MD, PhD**[1,5], **Matthew T. Patrick, PhD**[1], **Xianying Xing, MD**[1], **Grace Hile, MD**[1], **Christophe Piketty, MD PhD**[4], **Anne Lazzari, PhD**[4], **Wouter Van Delm, PhD**[4], **Emanual Maverakis, MD PhD**[6], **Mio Nakamura, MD**[1], **Robert L. Modlin, MD PhD**[7], **J. Michelle Kahlenberg, MD PhD**[8,9], **Allison C. Billi, MD PhD**[1], **Valerie Julia, PhD**[4], **Jayendra Kumar Krishnaswamy, PhD**[4], **Johann E. Gudjonsson, MD, PhD**[1,8,9,*]

[1.]Department of Dermatology, University of Michigan, Ann Arbor, MI, USA

[2.]Department of Biostatistics, University of Michigan, Ann Arbor, MI, USA

[3.]Department of Computational Medicine and Bioinformatics, University of Michigan, Ann Arbor, MI, USA

[4.]Galderma, Lausanne, Switzerland

[5.]Department of Pathology, University of Michigan, Ann Arbor, MI, USA

[6.]Department of Dermatology, University of California Davis, Sacramento, CA, USA

[7.]Department of Dermatology, University of California Los Angeles (UCLA), CA, USA

[8.]Department of Internal Medicine, Division of Rheumatology, University of Michigan Ann Arbor

[9.]Taubman Medical Research Institute.

Abstract

Background: Prurigo nodularis (PN) is a chronic neuroimmune skin disease characterized by bilaterally distributed pruritic hyperkeratotic nodules on extremities and trunk. Neuroimmune dysregulation and chronic scratching are believed to both induce and maintain the characteristic lesions.

Objective: To provide a comprehensive view of the molecular pathogenesis of PN at the single-cell level to identify and outline key pathologic processes and the cell types involved. Features that distinguish PN skin from the skin of patients with atopic dermatitis (AD) were of particular interest. We further aimed to determine the impact of the interleukin-31 (IL-31) receptor alpha antagonist, nemolizumab, and its specificity at the single-cell level.

[*]corresponding author. Johann E. Gudjonsson. johanng@med.umich.edu.

Method: Single-cell RNA-sequencing (scRNA-seq) of skin from 15 healthy donors and nonlesional and lesional skin from 6 patients each with PN and AD, combined with spatial-sequencing (spatial-seq) using the 10X Visium platform. Integration with bulk RNA-seq data from patients treated with nemolizumab.

Results: Our results demonstrate that PN is an inflammatory skin disease characterized by both keratinocyte proliferation and activation of profibrotic responses. We demonstrate that the *COL11A1+* fibroblast subset is a major contributor to fibrosis and is predominantly found in the papillary dermis of PN skin. Activation of fibrotic responses is the main distinguishing feature between PN and AD skin. We further show the broad effect of nemolizumab on PN cell types, with a prominent effect driving *COL11A1+* fibroblast and keratinocyte responses toward normal.

Conclusion: This study provides a high-resolution characterization of the cell types and cellular processes activated in PN skin, establishing PN as a chronic fibrotic inflammatory skin disease. It further demonstrates the broad effect of nemolizumab on pathological processes in PN skin.

Capsule Summary:

Prurigo Nodularis is characterized by immune shifts away from Th2 responses towards a pro-fibrotic state involving COL11A1+ fibroblasts and keratinocyte cross-talk, which is normalized upon targeting of the IL-31 receptor by nemolizumab.

Keywords

Prurigo nodularis; nemolizumab; fibrosis; inflammation; single-cell RNA-sequencing; spatial-sequencing

INTRODUCTION

Prurigo nodularis (PN) is a chronic neuroimmune skin disease characterized by chronic and intense pruritus with a marked impact on quality of life (1). Clinically it is characterized by multiple nodules that can cover large areas of the extremities and the trunk (2). The pathogenesis of PN remains unclear, but previous studies have implicated immune and neural dysregulation as critical circuits in its pathogenesis (3). PN has been suggested to have a clinical and pathologic overlap with atopic dermatitis (AD) (4) by which it may share a T helper 2 (Th2) polarization (5–7). However, a direct comparison of these two conditions has not yet been performed at a single-cell level. Indeed, in a previous study, Bulk-RNASeq analyses revealed that PN has a distinct molecular signature as compared to AD (8).
The best characterized immune mediator in PN is the cytokine IL-31 (9) receptor alpha (IL-31RA) and oncostatin M receptor beta (OSMRB) (10)Activated Th2 cells are considered the main IL-31 source, but other cell types can also produce IL-31, including eccrine sweat glands (11), mast cells (12), basophils (13), eosinophils (14–16), monocytes/macrophages (17, 18). A recent study in human PN lesions revealed that macrophages, in addition to T cells, are major cellular sources of IL-31 (19). The critical importance of IL-31 to PN pathogenesis has been demonstrated with nemolizumab, an investigational monoclonal antibody that inhibits IL-31RA (20) which leads to effective suppression of downstream inflammatory responses, including Th2 responses and stabilization of extracellular matrix (ECM) remodeling (8). Recently published evidence has indicated that fibrosis is a feature

of PN (8) (21), but the source of this fibrosis in PN skin is unknown. The major fibroblast populations in human skin have been described with the two major clusters characterized by the expression of SFRP2 and FMO1, with five minor fibroblasts defined including COL11A1+ fibroblast, with three (SFRP2+, FMO1+, and COL11A1+), based on their gene expression profiles, suggested to have a role in matrix deposition, inflammatory cell retention, and connective tissue cell differentiation (22).

Here we provide an in-depth exploration of PN pathogenesis to characterize the central mechanisms involved and identify the target cells of nemolizumab treatment, and contrast its pathogenesis with AD through a combination of single-cell RNA (scRNA) and spatial-RNA-sequencing approaches.

MATERIALS AND METHODS

Human sample acquisition

6 prurigo nodularis, 6 AD patients, and 15 healthy donors were recruited for single-cell RNA sequencing. 6mm punch biopsies were obtained from affected lesional and non-lesional AD and PN skin. Patients were not on active topical treatment at least 2 weeks prior to enrollment. No patient was on prior systemic treatment. Patients with PN did not have concomitant active AD. The study was approved by the University of Michigan Institutional Review Board (IRB), and all patients gave written consent. The study was conducted according to the Declaration of Helsinki Principles. See patient demographics in supplemental table 3. Patient cohort and data used from the nemolizumab clinical trial are as described in Tsoi et al (8).

Single-cell RNA-seq library preparation, sequencing, and alignment

Generation of single-cell suspensions for scRNA-seq was performed as follows: Skin biopsies were incubated overnight in 0.4% dispase (Life Technologies) in Hank's Balanced Saline Solution (Gibco) at 4°C. The epidermis and dermis were separated. The epidermis was digested in 0.25% Trypsin-EDTA (Gibco) with 10U/mL DNase I (Thermo Scientific) for 1 hour at 37°C, quenched with FBS (Atlanta Biologicals), and strained through a 70μM mesh. The dermis was minced, digested in 0.2% Collagenase II (Life Technologies) and 0.2% Collagenase V (Sigma) in a plain medium for 1.5 hours at 37°C, and strained through a 70μM mesh. Epidermal and dermal cells were combined in a 1:1 ratio, and the libraries were constructed by the University of Michigan Advanced Genomics Core on the 10X Chromium system with chemistry v3. Libraries were then sequenced on the Illumina NovaSeq 6000 sequencer to generate 150 bp paired-end reads. Data processing including quality control, read alignment (hg38), and gene quantification was conducted using the 10X Cell Ranger software. All transcriptomic data, including single-cell, is publicly available (GEO# pending).

Cell clustering and cell type annotation

The R package Seurat (v4.1.1) (23) was used to cluster the cells in the merged matrix. Cells with less than 500 transcripts or 100 genes or more than 1e5 transcripts or 10% of mitochondrial expression were first filtered out as low-quality cells. The

NormalizeData function was used to normalize the expression level for each cell with default parameters. The FindVariableFeatures function was used to select variable genes with default parameters. The ScaleData function was used to scale and center the counts in the dataset. Principal component analysis (PCA) was performed on the variable genes. The RunHarmony function from the Harmony package was applied to remove potential batch effects among samples processed in different batches. Uniform Manifold Approximation and Projection (UMAP) dimensional reduction was performed using the RunUMAP function. The clusters were obtained using the FindNeighbors and FindClusters functions with the resolution set to 0.6. The cluster marker genes were found using the FindAllMarkers function. The cell types were annotated by overlapping the cluster markers with the canonical cell type signature genes. To calculate the disease composition based on cell type, the number of cells for each cell type from each disease condition were counted. The counts were then divided by the total number of cells for each disease condition and scaled to 100 percent for each cell type. Differential expression analysis between any two groups of cells was carried out using the FindMarkers function. All differential expression analyses comparisons were displayed as average log2 fold-change, and corrected for multiple testing using false-discovery-rate (FDR) adjustment.

Cell type sub-clustering

Sub-clustering was performed on the abundant cell types. The same functions described above were used to obtain the sub-clusters. Sub-clusters that were defined exclusively by mitochondrial gene expression, indicating low quality, were removed from further analysis. The subtypes were annotated by overlapping the marker genes for the sub-clusters with the canonical subtype signature genes. The module scores were calculated using the AddModuleScore function on the intended gene lists. The ECM score was calculated on the genes from the extracellular matrix pathway from the Gene Ontology database. The cytokine score for fibroblast subtypes was calculated on induced genes in fibroblasts after stimulation with TGF-β or IL-4. The Nemolizumab induced or reduced genes were obtained from the previous bulk RNA-seq study by Tsoi *et al.* (8). Differentially expressed genes or cluster marker genes were used for enrichment analysis to obtain the potential upstream regulators using Ingenuity Pathway Analysis (QIAGEN Inc., https://www.qiagenbioinformatics.com/products/ingenuity-pathway-analysis) or canonical pathways using Enrichr.

Ligand receptor interaction analysis

CellphoneDB (v3) (24) and CellChat (25) were applied for ligand-receptor analysis [REF]. Each cell type was separated by its disease classifications (healthy, nonlesional, and lesional), and a separate run was performed for each disease classification. Pairs with p-value> 0.05 were filtered out from further analysis. The number of interactions between each cell type pair was then calculated for each condition. To compare the healthy and lesional conditions, the pairs that showed higher interaction score in the lesional condition were used to show the lesional-specific interactions.

Immunohistochemistry staining

Paraffin embedded tissue sections (lesional and healthy skin) were heated at 60°C for 30 minutes, de-paraffinized, and rehydrated. Slides were placed in PH9 antigen retrieval

buffer and heated at 125°C for 30 seconds in a pressure cooker water bath. After cooling, slides were treated with 3% H_2O_2 (5 minutes) and blocked using 10% goat serum (30 minutes). Overnight incubation (4°C) was then performed using anti-human primary antibody. Antibodies used were anti-COL11A1 (ThermoFisher Scientific, cat#PA5–68410), anti-SFRP2 (Lifespan Biosciences, cat#LS-C794043), anti-SFRP4 (Lifespan Biosciences, cat#LC-C408100), anti-TREM2 (ThermoFisher Scientific, cat#PA5–18763), anti-RAMP1 (Abcam, cat#AB64409), anti-CD4 (ThermoFisher Scientific, cat#14-244-82), anti-CD8 (ThermoFisher Scientific, cat#MA5–13473), anti-CD3 (Origene, cat#UM500048). Slides were then washed, and treated with secondary antibody, peroxidase (30 minutes), and diaminobenzidine substrate. Counterstain with Hematoxylin and dehydration was done, and slides were mounted and viewed under the microscope.

Spatial sequencing library preparation

Skin samples were frozen in OCT medium and stored at −80°C until sectioning. Optimization of tissue permeabilization was performed on 20 μm sections using Visium Spatial Tissue Optimization Reagents Kit (10X Genomics) which established an optimal permeabilization time to be 9 minutes. Samples were mounted onto a Gene Expression slide (10X Genomics), fixed in ice-cold methanol, stained with hematoxylin and eosin, and scanned under a microscope (Keyence). Tissue permeabilization was performed to release the poly-A mRNA for capture by the poly(dT) primers that are precoated on the slide and include an Illumina TruSeq Read, spatial barcode, and unique molecular identifier (UMI). Visium Spatial Gene Expression Reagent Kit (10X Genomics) was used for reverse transcription to produce spatially barcoded full-length cDNA and for second-strand synthesis followed by denaturation to allow a transfer of the cDNA from the slide into a tube for amplification and library construction. Visium Spatial Single Cell 3′ Gene Expression libraries consisting of Illumina paired-end sequences flanked with P5/P7 were constructed after enzymatic fragmentation, size selection, end repair, A-tailing, adaptor ligation, and PCR. Dual Index Kit TT Set A (10X Genomics) was used to add unique i7 and i5 sample indexes and generate TruSeq Read 1 for sequencing the spatial barcode and UMI and TruSeq Read 2 for sequencing the cDNA insert, respectively. Libraries were then sequenced on the Illumina NovaSeq 6000 sequencer to generate 150 bp paired-end reads.

Spatial sequencing data analysis

After sequencing, the reads were aligned to the human genome (hg38), and the expression matrix was extracted using the spaceranger pipeline (10X Genomics). Seurat was then used to analyze the expression matrix. Specifically, the SCTransform function was used to scale the data and find variable genes with default parameters. PCA and UMAP were applied for dimensional reduction. The FindTransferAnchors function was used to find a set of anchors between the spatial-seq data and scRNA-seq data, which were then transferred from the scRNA-seq to the spatial-seq data using the TransferData function. These two functions construct a weight matrix that defines the association between each query cell and each anchor. These weights sum to 1 for each spot and were used as the percentage of the cell type in the spot. The ECM score was calculated using the AddModuleScore function on the genes from the extracellular matrix pathway from the Gene Ontology database.

RESULTS

Single-cell RNA-seq and spatial-seq reveal diverse cell types and their spatial locations in PN skin

To understand the unbiased cellular composition and cell states of healthy (H) skin and lesional PN (LPN) skin, we generated single-cell suspensions of skin biopsies from 15 healthy donors and 6 patients with PN. We also collected skin biopsies from peripheral nonlesional sites from 4 out of the 6 PN patients (NPN), yielding a total 25 scRNA-seq libraries. The resulting quality-controlled PN plus healthy single-cell atlas contained a total of 72,782 cells, with an average of 2,379 genes and 10,417 transcripts detected per cell. To study the heterogeneity of these cells, we selected variable genes and performed uniform manifold approximation and projection (UMAP) dimensionality reduction and cell clustering using the R package Seurat (23). Cluster annotation was corroborated by overlapping the cluster markers with the canonical lineage-specific genes reported in previous skin disease scRNA-seq studies (26–30). We recovered 10 major cell types across all the samples (Figure 1A), including keratinocytes, melanocytes, eccrine gland cells, endothelial cells, fibroblasts, pericytes, nerve cells, T cells, myeloid cells, and mast cells. Most of these cell types contained cells from the majority of the healthy, NPN, and LPN libraries, suggesting that each cell type was associated with a common cell lineage rather than derived from a specific condition. Two small cell populations, eccrine gland cells and nerve cells were mainly derived from healthy samples. Interestingly, clear separations were observed in the keratinocytes, fibroblasts, and endothelial cells among the healthy, NPN, and LPN cells, suggesting major transcriptional differences (Figure 1B). Moderate shifts in terms of the proportion of cell types were seen in LPN compared to NPN and healthy, with the most pronounced shifts in mast cells, endothelial cells, T cells, and myeloid cells in LPN skin (Figure 1C). Marker genes for each cell population showed a clear separation between each cell type (Figure 1D).

To localize the major cell types detected by scRNA-seq in PN skin, we performed spatial sequencing (spatial-seq) on the PN skin sample using the 10X Visium platform. We detected 395 spatially defined spots with an average of 2,613 genes and 4,432 transcripts per spot (Supplemental Figure 1). We deconvoluted the spatial spots by the major cell types detected in scRNA-seq using the Seurat anchor-based label transfer method (see Methods). The prediction scores for each cell type were displayed on the tissue (Figure 1E) and combined into a scatter-pie plot representing the relative cell type composition for each spot (Supplemental Figure 1B). As expected, keratinocytes localized to the epidermis and the hair follicle. Myeloid cells and T cells were primarily located in the superficial dermis in proximity to the epidermis. Fibroblasts were distributed throughout a large proportion of the spots in the dermis, and the pericytes were located close to the blood vessels (Supplemental Figure 1B). These two cell types were the main producers of extracellular matrix (ECM) components (Supplemental Figure 1C). The other cell types represent small populations and were lowly detected in the spatial-seq sample.

COL11A1+ fibroblasts are enriched for pro-fibrotic responses in PN skin

To characterize the heterogeneity of the fibroblasts, we sub-clustered all the fibroblasts from the scRNA-seq dataset. Based on previously published marker genes (22), we annotated the fibroblast sub-clusters into six subtypes, including SFRP2+ fibroblasts (FB), APOE+ FB, RAMP1+ FB, COL11A1+ FB, TNN+ FB, and SFRP4+ FB (Figure 2A, and Supplemental Figure 1). Interestingly, COL11A1+ FB were mainly derived from the LPN samples compared to the healthy or NPN samples (Figure 2B, C). The COL11A1+ FB expressed high levels of *COL11A1*, *POSTN*, and *PRSS23*, suggesting a profibrotic role in PN skin (Figure 2D). To illustrate the capacity of ECM production by the different fibroblast subtypes, we calculated the ECM module score using the gene list from the extracellular matrix pathway from Gene Ontology and identified the highest ECM score in the LPN COL11A1+ FB (p=4.4E-83) (Figure 2E). We then performed differential expression analysis between the LPN and healthy COL11A+ FB and inferred the upstream regulators driving the differential expression. High activation z-score of TGFB1, IL-5, and IL-4 are likely reflective of pro-fibrotic responses, and high TNF, IFNG, and IL-6 activation z-scores suggest inflammatory response in the LPN COL11A1+ FB compared to healthy counterparts (Figure 2F). Enrichment analysis also revealed top fibrosis-related pathways (i.e., extracellular matrix organization, collagen fibril organization) and inflammation-related pathways (i.e., neutrophil degranulation, neutrophil activation involved in immune response) (Figure 2G). The COL11A1+ FB had the highest expression pattern of the collagen genes, including *COL1A1*, *COL1A2*, *COL3A1*, *COL5A1*, *COL5A2*, *COL6A1*, *COL6A2*, *COL6A3*, *COL11A1*, *COL12A1*, *COL14A1*, and *COL16A1* (Figure 2H). Taken together, the above results suggest a strong fibrotic potential for COL11A1+ FB in LPN skin. We confirmed the presence of the major fibroblast subtypes (SFRP4, SFRP2, RAMP1, and COL11A1 (see Figure 2I and Supplemental Figure 2) and validated the fibrosis phenotype by immunohistochemistry in PN skin. To compare the fibrosis-inducing capacity of the fibroblasts in PN and AD, we combined our PN scRNA-seq dataset with a single-cell dataset from AD skin and compared ECM scores among the fibroblast subtypes in healthy (H), nonlesional AD (NAD), NPN, lesional AD (LAD), and LPN skin. Although the LAD fibroblast subtype exhibited a higher ECM score compared to healthy or peripheral nonlesional fibroblasts, LPN fibroblast subtypes expressed a strikingly higher ECM score than the LAD cells (p=1.8×10–15) (Figure 2J), particularly in COL11A1+ FBs which was the FB subset most prominently increased in PN skin (p=2.2×10–9) (Figure 2K).

Endothelial cells and pericytes demonstrate fibrotic and inflammatory responses in PN skin

We next investigated the heterogeneity of the endothelial cells and clustered these cells into six sub-clusters (Figure 3A, B). Disease composition analysis identified that endothelial sub-cluster 2 and 5 were enriched in LPN compared to healthy or NPN samples (Figure 3C, D, p= 0.0014 and 2.1×10–22, respectively). Sub-cluster 2 represented the activated endothelial cells with high expression of *ICAM1* and E-selectin (*SELE*), which also display inflammatory features such as *TNFAIP3* and *IL6*. Sub-cluster 5 expressed high levels of several collagen genes (i.e., *COL4A1* and *COL15A1*), suggesting potential involvement in fibrosis (Figure 3B). To study these two LPN-specific sub-clusters, we performed enrichment analysis using their cluster marker genes. Sub-cluster 2 marker genes

implicated proinflammatory cytokines (i.e., *TNF*, *IL1B*, *IFNG*, *IL6*) and pathways (i.e., cytokine-mediated signaling pathway, cellular response to cytokine stimulus) (Figure 3E, F). Sub-cluster 5 marker genes were regulated by profibrotic upstream regulators (i.e., TGFB1, angiotensinogen (AGT), epidermal growth factor (EGF), IL-5) and enriched in ECM-related pathways (i.e., extracellular matrix organization, extracellular structure organization) (Figure 3G, H). These results suggest that endothelial cells were actively involved in both fibrotic and inflammatory responses in PN skin.

Similarly, we sub-clustered the pericytes and obtained nine sub-clusters (Supplementary Figure 3A, D). Composition analysis identified that sub-cluster 3 and sub-cluster 8 were enriched in LPN samples compared to healthy or NPN samples (Supplementary Figure 3B, C). We calculated the ECM score and plotted all the collagen genes across the pericyte subtypes. Cells in sub-cluster 3 had the highest ECM score in LPN and displayed the highest expression pattern of the collagen genes (Supplementary Figure 3E, F). LPN cells in sub-cluster 7 also revealed a much higher ECM score than the healthy cells, and expressed the second-highest pattern of collagen genes (Supplementary Figure 3E, F). We then performed enrichment analyses using the marker genes for sub-cluster 3 and sub-cluster 7 and found that both sub-clusters implicated in profibrotic upstream regulators (i.e., TGFB1, AGT, prolactin (PRL)) and pathways (i.e., extracellular matrix organization, collagen fibril organization) (Supplementary Figure 2G–J). Sub-cluster 3 also illustrated inflammatory response driven by interferon (Supplementary Figure 2, G, I). Taken together, these results demonstrate that endothelial cells and pericytes may actively contribute to fibrotic and inflammatory responses in lesional PN skin.

Keratinocyte responses in PN skin

We sub-clustered the keratinocytes and obtained six keratinocyte subtypes: basal, spinous, supraspinous, granular, follicular, and inflammatory keratinocytes (Figure 4A, D). The inflammatory keratinocytes were primarily derived from LPN samples (Figure 4B, C). Enrichment analysis using the inflammatory keratinocyte markers implicated proinflammatory upstream regulators and mitochondrial respiratory pathways, suggesting high energy consumption in PN keratinocytes during inflammation (Figure 4E). Upstream regulators of the inflammatory subtype of keratinocytes included the Th2 cytokines (IL-4, IL-5, IL-33), along with TGFB1 (Figure 4F), supportive of an enriched Th2 response in lesional PN skin.

scRNA-seq reveals immune subtype heterogeneity in PN skin

Given the strong inflammatory response observed in fibroblast, endothelial cells, and pericytes, the heterogeneity of immune cells was investigated. We sub-clustered and annotated the myeloid cells into nine subtypes, including cycling myeloid cells, Langerhans cells (LC), plasmacytoid dendritic cells (pDC) -, classical type 1 dendritic cells (cDC1), classical type 2 dendritic cells subset A (cDC2A), classical type 2 dendritic cells subset B (cDC2B), interstitial macrophages (IM), perivascular macrophage, and lipid-associated macrophages (LAM, also called TREM2 macrophage) (Supplemental Figure 4A–E, p-values for pDC, cDC2A, IM, PVM, and LAM were 1.30×10–13, 3.33×10–8, 1.72×10–12, 9.41×10–5, and 4.5×10–11, respectively). We observed an increased proportion of pDCs,

cDC2A, and macrophage subpopulations (IM, PVM, and LAM/TREM2) in lesional PN skin compared to non-lesional and healthy (Supplemental Figure 4D–E). The prominence of LAM/TREM2 macrophages in lesional PN skin was confirmed using immunohistochemistry (Supplemental Figure 4). For T cells and other lymphoid cells, we obtained seven subtypes: cycling T cells, innate lymphoid cells (ILC), natural killer cells (NK), CD8+ T cells (CD8T), tissue-resident memory T cells (Trm), CD4+ T cells (CD4T), and regulatory T cells (Treg). Several NK and T cell populations showed increased proportion in lesional PN skin including cycling, NK, CD8, and T regulatory cells. We confirmed the presence of T cells in lesional PN skin by IHC staining for CD8 and CD4 (Supplemental Figure 4).

Ligand-receptor analysis reveals cell type-specific networks in PN

To address the observed shifts in cell type composition and transcriptional changes, we analyzed how cell-cell communication changes in PN compared to healthy skin. To do this, we performed separate ligand-receptor analyses on the healthy, NPN, and LPN cell types using CellphoneDB and CellChat. The greatest number of interactions were observed in LPN (Figure 5C) compared to the healthy (Figure 5A) or NPN skin (Figure 5B), particularly among fibroblasts, endothelial cells, pericytes, myeloid cells, and keratinocytes. To study the specific ligand-receptor pairs in PN, we selected the pairs that had higher interaction scores in LPN compared to healthy or NPN, which uncovered various signaling pathways implicated in PN arising from both immune (T cell, myeloid) and stromal cell populations (fibroblasts, endothelial cells, and pericytes). Several validated proinflammatory cytokines, such as *IFNG*, *IL1*, *IL6*, and *TNF*, were also involved in PN pathogenesis. Notably, our analysis revealed several other proinflammatory mediators, including *CCL2*, *CCL3*, *CXCL2*, *CXCL12*, and *IL7*, that were expressed by various cell types in PN skin (Figure 5D, E). The emergence of fibroblast growth factor (*FGF2*, *FGF7*), platelet-derived growth factor (*PDGFB*), transforming growth factor beta (*TGFB1*, *TGFB2*, *TGFB3*), and vascular endothelial growth factor (VEGFB) corroborated involvement of fibrosis in PN pathogenesis. A robust signaling network was observed related to the TGFB signaling pathway in lesional PN skin with the source of TGFB observed in multiple cell types and the main target cell in LPN skin being fibroblasts (Figure 5F). Taken together, these data illustrate profibrotic and proinflammatory shifts within the interactome in PN skin.

Comparison between epithelial responses in PN versus AD skin by single-cell analyses.

As mentioned previously, lesional PN skin showed an expansion of COL11A1 fibroblasts as compared to lesional AD skin, suggesting a more pro-fibrotic signature in PN pathophysiology (Figure 2J and Supplemental Figure 2B). We further compared keratinocyte responses in PN and AD skin and compared gene expression changes in each compartment (Supplemental Figure 5A–D). Both PN and AD skin had an expansion of KCs in cluster 3 which corresponded to an “inflammatory” phenotype with prominent expression of several inflammatory markers including *KRT6* and *KRT16*, *S100A8/A9*, along with IFN signature genes such as *IFI27*, *IFITM3*, and the inflammasome gene *PYCARD* encoding apoptosis-associated speck-like protein containing a CARD (ASC) (Supplemental Figure 5A, D, E). Assessing enriched gene ontology categories in each KC compartment using a threshold of FC>2, and FDR<0.05, demonstrated fairly consistent changes across the “inflammatory”, basal, spinous, supraspinous, and follicular keratinocytes, with AD having

enriched inflammatory responses such as “defense response to bacterium” and “neutrophil degranulation” (p=2.8xE-07 and p=3.8xE-05, respectively), in “inflammatory” KCs), and T-cell chemotaxis in basal, and spinous AD KCs (p=3.5×10E-05, p=4.1×10E-5, respectively) compared to PN skin (Supplemental Figure 5F). In contrast, terms associated with altered epidermal differentiation were enriched in “inflammatory” and spinous keratinocytes from PN as compared to AD skin (Supplemental Figure 5F). Consistent in all KC subtypes was higher expression of the chemokine *CCL27*, *S100A7*, and *S100A9* in AD compared to PN.

Comparison of immune cell responses in PN versus AD skin by single-cell analyses.

The proportion of T cell subsets was overall similar between PN and AD skin, across several T cell subsets including CD8, and CD4 effector T cells, Tregs, and cycling T cells. In addition, prominent ILC and NK cell subsets were present in both NPN, LPN, NAD, and LAD skin (Supplemental Figure 6A–D). Most prominent differences between LAD and LPN skin were found in CD4+ effector T cells, with LAD CD4+ cells having increased expression of *IL13* (2.7-fold higher, FDR=8.5×10–24), and *IL22* (4.7-fold, FDR=6.0×10–21) (Supplemental Table 1). Very Few *IL4* positive T cells were observed in LAD skin (Supplemental Figure 7). In contrast, LPN CD4+ T cells had higher expression of *CCL5* (2.4-fold, FDR=2.8×10–16). There was a trend towards increased expression of *IL17A* and *IL17F* in LPN compared to LAD skin, but this was not significant (Supplemental Figure 7).

We identified the same 9 myeloid cell subsets as above in PN, AD, and healthy skin with several subsets being more prominent in LPN skin compared to LAD (Supplemental Figure 6 E–H). This included pDCs, interstitial macrophages (IM), and lipid-associated macrophages (LAM, *TREM2*$^{+}$). Most prominent differences in gene expression were found in PN IM macrophages, which had increased expression of *CCL3* and *CCL4* (2.7-fold for both, FDR=2.0×10–9 and 3.9×10–5, respectively). In contrast, LAD IM macrophages had increased expression of MHC class II molecules including *HLA-DRB1*, *HLA-DQA1*, and *HLA-DQB1* (2.2-, 2.3-, and 2.7-fold, and FDR=2.7×10–10, =8.6×10–14, =9.8×10–13, respectively) (Supplemental Table 2).

IL-31 receptor alpha blockade with nemolizumab reverts the transcription profile in LPN fibroblasts and keratinocytes toward healthy

We have previously demonstrated transcriptomic changes using a bulkRNA-seq approach in PN skin following treatment with the IL-31 receptor alpha antagonist, nemolizumab (8). To determine where the biological response of nemolizumab is most prominent, we plotted the expression of the two genes encoding for the heterodimeric IL-31 receptor, i.e IL-31RA and OSMRB (Figure 6A, B). *IL31RA* was specifically expressed in fibroblasts and keratinocytes. In contrast, *OSMRB* was more widely expressed in fibroblasts, keratinocytes, pericytes, and endothelial cells. Strikingly, genes that were differentially upregulated with nemolizumab treatment compared to baseline lesional were predominantly found in the fibroblast cluster, whereas genes that were differentially downregulated localized more broadly to keratinocytes and immune cell subsets, consistent with attenuation of hyperkeratosis and decreased inflammatory responses with treatment (Figure 6C, D). To study the effects of nemolizumab on the gene expression levels down to the single-cell level in PN skin, we generated a list from a recently published bulk RNA-seq study, containing

genes significantly downregulated by nemolizumab as compared to placebo (8). We then calculated module scores using the gene list across all major cellular subtypes in PN skin (Figure 6D), KC subsets (Figure 6E), and FB subsets (Figure 6F). Consistent with the expression of IL31RA and OSMR, the most pronounced changes were observed in keratinocytes and fibroblasts, particularly inflammatory KCs and the COL11A1+ fibroblasts. These results indicate that nemolizumab treatment reverts the transcription profile from PN towards healthy skin in a broad range of both stromal and immune cell populations, particularly in fibroblasts and keratinocytes, the cell types responsible for the most pronounced histopathologic changes in lesional PN skin.

DISCUSSION

This study provides a detailed insight into the pathogenesis of PN, and the associated tissue-specific and cell-type specific changes that occur in PN skin. Strikingly, changes in PN skin are observed across both immune and stromal cell populations, including keratinocytes, endothelial cells, and most profoundly fibroblasts and fibroblast subpopulations, with increased profibrotic responses being the key distinguishing features of PN from AD, accompanied by an immune shift away from IL-13 and IL-22 responses.

A characteristic histopathologic feature of PN is fibrosis of the papillary dermis with vertically arranged collagen fibers (31). Our findings are consistent with this well-known characteristic, showing a marked increase in dense collagen in the papillary dermis in lesional PN skin by trichrome staining and increased expression of pro-collagen I in the papillary dermis. Moreover, through our single-cell analyses, we identified the *COL11A1+* fibroblast subset as the major source of activated and enriched profibrotic responses, including increased mRNA expression of both collagen I and collagen III. Consistent with their profibrotic function, *COL11A1+* fibroblasts were primarily found in the papillary dermis, where the fibrotic response was most marked with either trichrome or pro-collagen I staining indicative of active collagen I biosynthesis. This expansion of the *COL11A1+* fibroblast subpopulation is unique to PN and not seen in AD skin. Furthermore, the profibrotic effect of this population was not observed in AD *COL11A1+* fibroblasts. Recently a subset of cancer-associated fibroblast (CAF)-like-phenotype was described in AD skin (32) characterized by the expression of WNT5a, tenascin (TCN), and periostin (POSTN) amongst several other genes. In alignment with this publication, periostin (POSTN) and WNT5A were expressed in COL11A1+ fibroblasts in our dataset, along with fibroblast activation protein (FAP), a hallmark marker of CAF (33). Another recently published paper described CXCL14- IL24+ secretory-papillary dermis fibroblast as being unique to PN skin (34). We observe similar IL24+ CXCL14- negative FBs as a small subset with SFRP2+ FBs, and observed their enrichment in PN skin, but detectable levels in both lesional AD and healthy skin. These FBs expressed increased levels of MMP1 but lower levels of COL1A1 and COL1A2, suggesting that they do not contribute to fibrosis in PN skin.

Of the two components of the heterodimeric IL-31 receptor, *IL31RA* expression was detected on both keratinocytes and fibroblasts, whereas *OSMRB* expression was found to be more widespread in different cell populations. This suggests that the two key cell types

responding to IL-31 in PN are likely fibroblasts and keratinocytes, which is in keeping with our previous observation of the transcriptomic shifts driven by nemolizumab that can be attributed to those two cell types (8).

Notably, we observed evidence that other cell types including endothelial cells and pericytes also contribute to fibrosis in LPN skin. Endothelial changes are known in LPN (31) but the nature of these shifts has not been previously detailed. Our data suggest that endothelial cells, likely under the action of proinflammatory and profibrotic cytokines such as TGFB, contribute to extracellular matrix reorganization. Whether TGFb is the critical upstream promoter of fibrosis in PN remains to be determined but we observed TGFb being expressed in a wide range of cell types in PN skin including endothelial cells, fibroblasts, and nerve cells for *TGFB1*, and fibroblasts and pericytes for *TGFB2* and *TGFB3*. Notably, TGFB2 and TGFB3 have been more strongly implicated in fibrosis than TGFB1 based on recently published work (35).

One of the most characteristic histologic features of PN is the presence of compact orthohyperkeratosis, with irregular epidermal hyperplasia (31). As expected, keratinocytes demonstrated marked transcriptomic changes in lesional PN skin with the most marked shifts seen in inflammatory keratinocytes, defined by *KRT6*, *KRT16*, and *KRT17* along with *S100A8* and *S100A9* expression, and with our analyses indicating a key role of IL-13 and IL-22 cytokines in this transition, consistent with previous observations (36). The most enriched biological categories in the inflammatory keratinocyte subset had to do with mitochondrial function and protein translation suggesting the generation of reactive oxygen species and cellular stress that can contribute to inflammatory responses in the skin (37).

Immune cell infiltrate was prominently observed in lesional PN skin and was characterized by shifts in specific immune cell populations. The most pronounced shifts were observed in macrophage populations, particularly lipid-associated macrophages characterized by the expression of *APOE* and *TREM2*. The lipid metabolic products from lipid-associated macrophages have been shown to trigger the production of proinflammatory cytokines in atherosclerosis, which in turn amplify inflammatory responses (38). These macrophages have recently been implicated in the pathogenesis of acne (30). T cells were also prominent in PN lesions, with an increased number of cycling T cells, as well as NK, $CD8^+$, and Tregs. The role of these T cell populations in PN skin has not been previously characterized. Furthermore, various stromal cell populations, particularly endothelial and pericytes, had increased expression of various proinflammatory cytokines, chemokines, and adhesion molecules, suggesting an active role in immune trafficking and immune amplification in PN. This includes increased expression of the adhesion molecule *ICAM1*(39), E-selectin (*SELE*), and *IL6* in endothelial cells, and *CCL2*, *CCL3*, CCL4, CCL13, CCL18, *CXCL2*, and *CXCL12* that were expressed by myeloid, pericytes and endothelial cells in PN skin. It is noteworthy that CCL2 and IL-6 have established roles in the development of fibrosis (40). CCL2 is the most potent profibrotic chemokine; through CCR2, CCL2 acts directly on fibroblasts stimulating collagen synthesis. Likewise, IL-6 trans-signaling enhances lung fibroblast proliferation and extracellular matrix protein production (41).

Our data further outline differences between PN and AD. Notably, the shifts in cell populations in the epidermis are highly similar between both PN and AD with both diseases having a prominent “inflammatory” keratinocyte subset characterized by the expression of pro-inflammatory molecules including S100A8 and *S100A9* along with increased expression of the inflammatory keratins *KRT6* and *KRT16*. Changes in the expression of *S100A8* (42), *S100A9* (42, 43), and *KRT16* (44) have been described in AD skin, but their expression has not been addressed in PN skin. Interestingly, the epidermal changes were accompanied by subtle changes in the gene expression in PN vs. AD skin, with immune-related processes such as antimicrobial responses, and regulators of T cell trafficking only observed in LAD, but not LPN keratinocytes. We also observed changes in T cell phenotype between LPN and LAD skin, particularly within the CD4 effector T cell population, where mRNA expression of *IL13* and *IL22* was markedly lower in LPN skin compared to LAD skin. IL-22 is known to promote epidermal proliferation and activate innate immune and antimicrobial responses in the skin (45). IL-13 is a key effector cytokine in AD skin (46), and the therapeutic target of three biologics, IL4Rα blocker dupilumab, and the anti-IL13 lebrikizumab and tralokinumab mAbs (47). These data suggest, that while PN is an inflammatory-driven disease, it may not be centered around IL-13/IL-22 responses to the same degree as AD.

These data also provide information regarding the mechanisms of action of the IL-31 receptor antagonist, nemolizumab. In a previously published study, we performed a bulkRNA-seq analysis of LPN skin from patients treated with nemolizumab and observed transcriptomic shifts indicating stabilization of extracellular matrix remodeling and normalization of epidermal differentiation (8). Through cross-referencing the single-cell data with the nemolizumab bulkRNA-seq data we mapped out the broad effect of nemolizumab on the abnormal transcriptomic activation of various cell types in PN skin. Thus, the therapeutic effect and normalization of the pathologic transcriptomic signatures we observe in the COL11A1+ fibroblasts, and the inflammatory keratinocyte subset, likely reflect the observed clinical improvement of PN skin lesions during nemolizumab treatment (20). These results also validate our previous observations on the molecular and cellular impact of nemolizumab treatment on pathophysiological pillars of PN disease including, inflammation, altered epidermal differentiation, and fibrosis (20). Recently, treatment with the anti-IL-4R biologic dupilumab has been shown to be effective for the treatment of PN (48) suggesting that targeting Th2 inflammation in PN is effective. However, its molecular mechanisms in PN remain unexplored preventing a direct comparison against nemolizumab.

In summary, these data provide a unique insight into the pathogenesis of PN, highlighting PN as a chronic neuroimmune skin disease with complex immune-stromal cell crosstalk, promoting and likely driving abnormal keratinocyte proliferation and activation. This is accompanied by a marked shift towards a profibrotic response primarily within the papillary dermis involving activation of *COL11A1+* fibroblasts, endothelial cells, and pericytes. Remarkably, these changes are reversible by blocking IL-31 receptor alpha. Therefore, these novel insights expand our understanding of the pathogenesis of PN and the mode of action of anti-IL-31R therapy for this debilitating disease.

Supplementary Material

Refer to Web version on PubMed Central for supplementary material.

ACKNOWLEDGEMENT

This study was supported by Galderma SA. J.E. Gudjonsson and L.C. Tsoi are supported by the Babcock Endowment Fund, the National Institute of Health (P30-AR075043, K01-AR072129), and together with J.M. Kahlenberg, and Lam C. Tsoi, by the A. Alfred Taubman Medical Research Institute (J.E.G, J.M.K., L.C.T.).

Disclosures:

Disclosure of potential conflict of interest: J. E. Gudjonsson has served as a consultant to Almirall, BMS, Sanofi, AbbVie, Novartis, Eli Lilly, Pfizer, and Galderma; and has received research support from Almirall, Janssen, Novartis, Pfizer, BMS/Celgene, Timberpharma, and Galderma. J. M. Kahlenberg has received grant support from Q32 Bio, Celgene/BMS, Ventus Therapeutics, ROME therapeutics, and Janssen; and has served on advisory boards for AstraZeneca, Eli Lilly, GlaxoSmithKline, Bristol Myers Squibb, Avion Pharmaceuticals, Provention Bio, Aurinia Pharmaceuticals, Ventus Therapeutics, Gilead, and EMD Serano. M. Nakamura has received research support from Amgen, Argenx, BMS, Pfizer, and Regeneron. P. Chaskar, A. Lazzari, C. Piketty, W. Van Delm, V. Julia, and J. K. Krishnaswamy are employees of Galderma. The rest of the authors declare no relevant conflicts of interest.

Abbreviations:

AD	Atopic Dermatitis
cDC1	classical type 1 dendritic cell
APOE	apolipoprotein E
cDC2A	classical type 2 dendritic cell subset A
cDC2B	classical type 2 dendritic cell, subset B
CCL	C-C motif chemokine
COL	Collagen
ECM	extracellular matrix
CXCL	C-X-C motif chemokine ligand
FGF	fibroblast growth factor
FMO1	flavin-containing dimethylaniline monooxygenase 1
H	Healthy
IFN	interferon
IL	Interleukin
IM	Interstitial macrophages
KRT	keratin
LAM	lipid-associated macrophages

LAD	Lesional Atopic Dermatitis
LC	Langerhans cells
LPN	Lesional Prurigo Nodularis
NADL	non-lesional atopic dermatitis
NPN	non-lesional prurigo nodularis
OSMRB	oncostatin-M receptor B
pDC	plasmacytoid dendritic cells
PDGF	platelet-derived growth factor
PN	Prurigo Nodularis
POSTN	periostin
PRSS23	serine protease 23
PVM	perivascular macrophages
RAMP1	Receptor activity modifying protein 1
RNA	ribonucleic acid
scRNA-seq	single-cell RNA-seq
SFRP2	secreted frizzled-related protein 2
TGF	transforming growth factor
TNF	tumor necrosis factor
TNN	tenascin N
VEGF	vascular endothelial growth factor

REFERENCES

1. Janmohamed SR, Gwillim EC, Yousaf M, Patel KR, Silverberg JI. The impact of prurigo nodularis on quality of life: a systematic review and meta-analysis. Arch Dermatol Res. 2021;313(8):669–77. [PubMed: 33108524]
2. Huang AH, Williams KA, Kwatra SG. Prurigo nodularis: Epidemiology and clinical features. J Am Acad Dermatol. 2020;83(6):1559–65. [PubMed: 32454098]
3. Williams KA, Huang AH, Belzberg M, Kwatra SG. Prurigo nodularis: Pathogenesis and management. J Am Acad Dermatol. 2020;83(6):1567–75. [PubMed: 32461078]
4. Iking A, Grundmann S, Chatzigeorgakidis E, Phan NQ, Klein D, Stander S. Prurigo as a symptom of atopic and non-atopic diseases: aetiological survey in a consecutive cohort of 108 patients. J Eur Acad Dermatol Venereol. 2013;27(5):550–7. [PubMed: 22364653]
5. Calugareanu A, Jachiet M, Lepelletier C, De Masson A, Rybojad M, Bagot M, et al. Dramatic improvement of generalized prurigo nodularis with dupilumab. J Eur Acad Dermatol Venereol. 2019;33(8):e303–e4. [PubMed: 30893496]

6. Mollanazar NK, Elgash M, Weaver L, Valdes-Rodriguez R, Hsu S. Reduced Itch Associated With Dupilumab Treatment In 4 Patients With Prurigo Nodularis. JAMA Dermatol. 2019;155(1):121–2. [PubMed: 30427989]
7. Beck KM, Yang EJ, Sekhon S, Bhutani T, Liao W. Dupilumab Treatment for Generalized Prurigo Nodularis. JAMA Dermatol. 2019;155(1):118–20. [PubMed: 30427994]
8. Tsoi LC, Hacini-Rachinel F, Fogel P, Rousseau F, Xing X, Patrick MT, et al. Transcriptomic characterization of prurigo nodularis and the therapeutic response to nemolizumab. J Allergy Clin Immunol. 2022;149(4):1329–39. [PubMed: 34857395]
9. Sonkoly E, Muller A, Lauerma AI, Pivarcsi A, Soto H, Kemeny L, et al. IL-31: a new link between T cells and pruritus in atopic skin inflammation. J Allergy Clin Immunol. 2006;117(2):411–7. [PubMed: 16461142]
10. Zhang Q, Putheti P, Zhou Q, Liu Q, Gao W. Structures and biological functions of IL-31 and IL-31 receptors. Cytokine Growth Factor Rev. 2008;19(5–6):347–56. [PubMed: 18926762]
11. Dai X, Okazaki H, Hanakawa Y, Murakami M, Tohyama M, Shirakata Y, et al. Eccrine sweat contains IL-1alpha, IL-1beta and IL-31 and activates epidermal keratinocytes as a danger signal. PLoS One. 2013;8(7):e67666. [PubMed: 23874436]
12. Niyonsaba F, Ushio H, Hara M, Yokoi H, Tominaga M, Takamori K, et al. Antimicrobial peptides human beta-defensins and cathelicidin LL-37 induce the secretion of a pruritogenic cytokine IL-31 by human mast cells. J Immunol. 2010;184(7):3526–34. [PubMed: 20190140]
13. Raap U, Gehring M, Kleiner S, Rudrich U, Eiz-Vesper B, Haas H, et al. Human basophils are a source of - and are differentially activated by - IL-31. Clin Exp Allergy. 2017;47(4):499–508. [PubMed: 28000952]
14. Hashimoto T, Kursewicz CD, Fayne RA, Nanda S, Shah SM, Nattkemper L, et al. Pathophysiologic mechanisms of itch in bullous pemphigoid. J Am Acad Dermatol. 2020;83(1):53–62. [PubMed: 31351883]
15. Rudrich U, Gehring M, Papakonstantinou E, Illerhaus A, Engmann J, Kapp A, et al. Eosinophils are a Major Source of Interleukin-31 in Bullous Pemphigoid. Acta Derm Venereol. 2018;98(8):766–71. [PubMed: 29693698]
16. Kunsleben N, Rudrich U, Gehring M, Novak N, Kapp A, Raap U. IL-31 Induces Chemotaxis, Calcium Mobilization, Release of Reactive Oxygen Species, and CCL26 in Eosinophils, Which Are Capable to Release IL-31. J Invest Dermatol. 2015;135(7):1908–11. [PubMed: 25789701]
17. Hashimoto T, Yokozeki H, Karasuyama H, Satoh T. IL-31-generating network in atopic dermatitis comprising macrophages, basophils, thymic stromal lymphopoietin, and periostin. J Allergy Clin Immunol. 2022.
18. Hashimoto T, Kursewicz CD, Fayne RA, Nanda S, Shah SM, Nattkemper L, et al. Mechanisms of Itch in Stasis Dermatitis: Significant Role of IL-31 from Macrophages. J Invest Dermatol. 2020;140(4):850–9 e3. [PubMed: 31626785]
19. Hashimoto T, Nattkemper LA, Kim HS, Kursewicz CD, Fowler E, Shah SM, et al. Itch intensity in prurigo nodularis is closely related to dermal interleukin-31, oncostatin M, IL-31 receptor alpha and oncostatin M receptor beta. Exp Dermatol. 2021;30(6):804–10. [PubMed: 33428793]
20. Stander S, Yosipovitch G, Legat FJ, Lacour JP, Paul C, Narbutt J, et al. Trial of Nemolizumab in Moderate-to-Severe Prurigo Nodularis. N Engl J Med. 2020;382(8):706–16. [PubMed: 32074418]
21. Deng J, Parthasarathy V, Marani M, Bordeaux Z, Lee K, Trinh C, et al. Extracellular matrix and dermal nerve growth factor dysregulation in prurigo nodularis compared to atopic dermatitis. Front Med (Lausanne). 2022;9:1022889.
22. Tabib T, Morse C, Wang T, Chen W, Lafyatis R. SFRP2/DPP4 and FMO1/LSP1 Define Major Fibroblast Populations in Human Skin. J Invest Dermatol. 2018;138(4):802–10. [PubMed: 29080679]
23. Butler A, Hoffman P, Smibert P, Papalexi E, Satija R. Integrating single-cell transcriptomic data across different conditions, technologies, and species. Nat Biotechnol. 2018;36(5):411–20. [PubMed: 29608179]
24. Efremova M, Vento-Tormo M, Teichmann SA, Vento-Tormo R. CellPhoneDB: inferring cell-cell communication from combined expression of multi-subunit ligand-receptor complexes. Nat Protoc. 2020;15(4):1484–506. [PubMed: 32103204]

25. Jin S, Guerrero-Juarez CF, Zhang L, Chang I, Ramos R, Kuan CH, et al. Inference and analysis of cell-cell communication using CellChat. Nat Commun. 2021;12(1):1088. [PubMed: 33597522]
26. Gudjonsson JE, Tsoi LC, Ma F, Billi AC, van Straalen KR, Vossen A, et al. Contribution of plasma cells and B cells to hidradenitis suppurativa pathogenesis. JCI Insight. 2020;5(19).
27. Hughes TK, Wadsworth MH 2nd, Gierahn TM, Do T, Weiss D, Andrade PR, et al. Second-Strand Synthesis-Based Massively Parallel scRNA-Seq Reveals Cellular States and Molecular Features of Human Inflammatory Skin Pathologies. Immunity. 2020;53(4):878–94 e7. [PubMed: 33053333]
28. Ma F, Hughes TK, Teles RMB, Andrade PR, de Andrade Silva BJ, Plazyo O, et al. The cellular architecture of the antimicrobial response network in human leprosy granulomas. Nat Immunol. 2021;22(7):839–50. [PubMed: 34168371]
29. Billi AC, Ma F, Plazyo O, Gharaee-Kermani M, Wasikowski R, Hile GA, et al. Nonlesional lupus skin contributes to inflammatory education of myeloid cells and primes for cutaneous inflammation. Sci Transl Med. 2022;14(642):eabn2263.
30. Do TH, Ma F, Andrade PR, Teles R, de Andrade Silva BJ, Hu C, et al. TREM2 macrophages induced by human lipids drive inflammation in acne lesions. Sci Immunol. 2022;7(73):eabo2787.
31. Weigelt N, Metze D, Stander S. Prurigo nodularis: systematic analysis of 58 histological criteria in 136 patients. J Cutan Pathol. 2010;37(5):578–86. [PubMed: 20002240]
32. Patel JR, Joel MZ, Lee KK, Kambala A, Cornman H, Oladipo O, et al. Single-cell RNA sequencing reveals dysregulated fibroblast subclusters in prurigo nodularis. bioRxiv. 2023.
33. Han C, Liu T, Yin R. Biomarkers for cancer-associated fibroblasts. Biomark Res. 2020;8(1):64. [PubMed: 33292666]
34. Alkon N, Assen FP, Arnoldner T, Bauer WM, Medjimorec MA, Shaw LE, et al. Single-cell RNA sequencing defines disease-specific differences between chronic nodular prurigo and atopic dermatitis. J Allergy Clin Immunol. 2023.
35. Sun T, Huang Z, Liang WC, Yin J, Lin WY, Wu J, et al. TGFbeta2 and TGFbeta3 isoforms drive fibrotic disease pathogenesis. Sci Transl Med. 2021;13(605).
36. Fukushi S, Yamasaki K, Aiba S. Nuclear localization of activated STAT6 and STAT3 in epidermis of prurigo nodularis. Br J Dermatol. 2011;165(5):990–6. [PubMed: 21711341]
37. Sabnam S, Rizwan H, Pal S, Pal A. CEES-induced ROS accumulation regulates mitochondrial complications and inflammatory response in keratinocytes. Chem Biol Interact. 2020;321:109031. [PubMed: 32142722]
38. Tedgui A, Mallat Z. Cytokines in atherosclerosis: pathogenic and regulatory pathways. Physiol Rev. 2006;86(2):515–81. [PubMed: 16601268]
39. Hubbard AK, Rothlein R. Intercellular adhesion molecule-1 (ICAM-1) expression and cell signaling cascades. Free Radic Biol Med. 2000;28(9):1379–86. [PubMed: 10924857]
40. Luzina IG, Todd NW, Sundararajan S, Atamas SP. The cytokines of pulmonary fibrosis: Much learned, much more to learn. Cytokine. 2015;74(1):88–100. [PubMed: 25543535]
41. Le TT, Karmouty-Quintana H, Melicoff E, Le TT, Weng T, Chen NY, et al. Blockade of IL-6 Trans signaling attenuates pulmonary fibrosis. J Immunol. 2014;193(7):3755–68. [PubMed: 25172494]
42. Sugiura H, Ebise H, Tazawa T, Tanaka K, Sugiura Y, Uehara M, et al. Large-scale DNA microarray analysis of atopic skin lesions shows overexpression of an epidermal differentiation gene cluster in the alternative pathway and lack of protective gene expression in the cornified envelope. Br J Dermatol. 2005;152(1):146–9. [PubMed: 15656815]
43. Jin S, Park CO, Shin JU, Noh JY, Lee YS, Lee NR, et al. DAMP molecules S100A9 and S100A8 activated by IL-17A and house-dust mites are increased in atopic dermatitis. Exp Dermatol. 2014;23(12):938–41. [PubMed: 25308296]
44. Ghosh D, Ding L, Sivaprasad U, Geh E, Biagini Myers J, Bernstein JA, et al. Multiple Transcriptome Data Analysis Reveals Biologically Relevant Atopic Dermatitis Signature Genes and Pathways. PLoS One. 2015;10(12):e0144316.
45. Eyerich S, Eyerich K, Pennino D, Carbone T, Nasorri F, Pallotta S, et al. Th22 cells represent a distinct human T cell subset involved in epidermal immunity and remodeling. J Clin Invest. 2009;119(12):3573–85. [PubMed: 19920355]

46. Tsoi LC, Rodriguez E, Degenhardt F, Baurecht H, Wehkamp U, Volks N, et al. Atopic Dermatitis Is an IL-13-Dominant Disease with Greater Molecular Heterogeneity Compared to Psoriasis. J Invest Dermatol. 2019;139(7):1480–9. [PubMed: 30641038]

47. Zhang Y, Jing D, Cheng J, Chen X, Shen M, Liu H. The efficacy and safety of IL-13 inhibitors in atopic dermatitis: A systematic review and meta-analysis. Front Immunol. 2022;13:923362. [PubMed: 35967348]

48. Yosipovitch G, Mollanazar N, Stander S, Kwatra SG, Kim BS, Laws E, et al. Dupilumab in patients with prurigo nodularis: two randomized, double-blind, placebo-controlled phase 3 trials. Nat Med. 2023;29(5):1180–90. [PubMed: 37142763]

Key Messages

- Prurigo nodularis (PN) is an inflammatory skin disease with a shift away from Th2 responses.
- COL11A1 fibroblasts have the largest contribution to fibrotic responses in PN skin
- Nemolizumab, an IL-31R alpha blocker reverts the transcription profile toward healthy in PN fibroblasts and keratinocytes

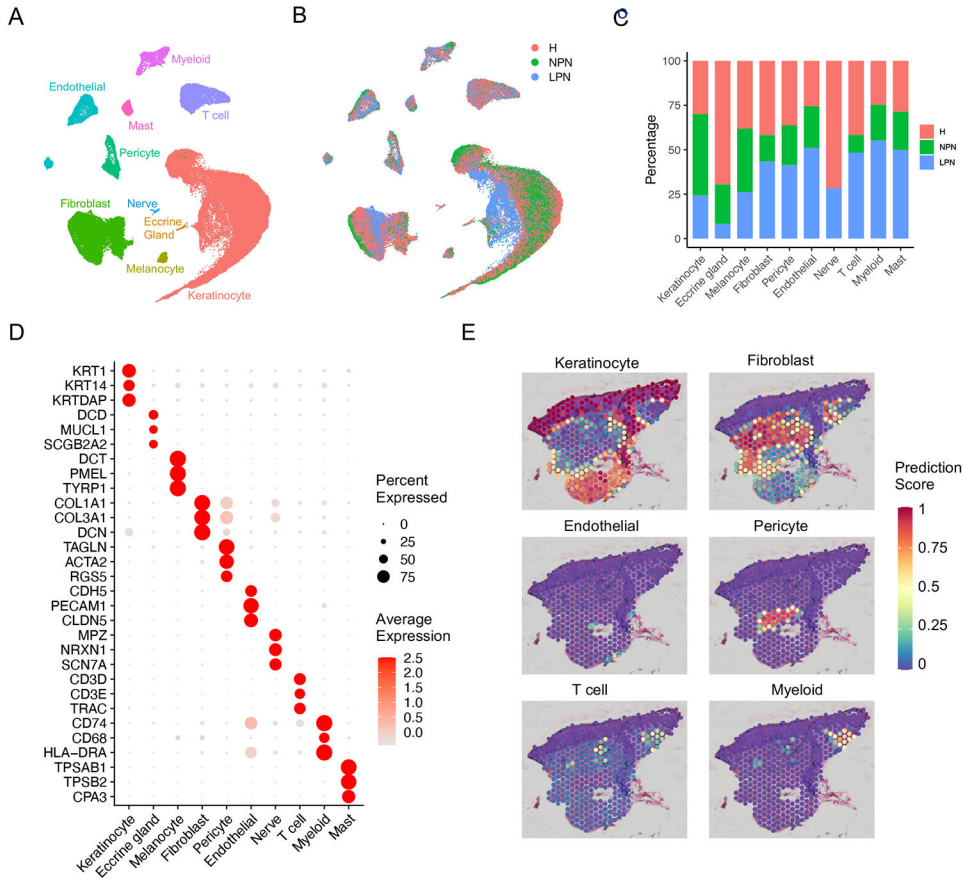

Fig. 1. Cell types observed in PN skin and their spatial locations.

A. UMAP plot showing 72,782 cells colored by cell types.

B. UMAP plot showing the cells colored by skin conditions. H: healthy control; NPN: nonlesional samples from patients with PN; LPN: lesional samples from patients with PN.

C. Bar plot showing the abundance composition across the skin conditions for each cell type in scRNA-seq.

D. Dot plot showing representative marker genes for each cell type. The color scale represents the scaled expression of each gene. The size of the dot represents the percentage of cells expressing each gene of interest.

E. Spatial plot showing the deconvolution score for each cell type. The coordinates of the spot correspond to the location in the tissue.

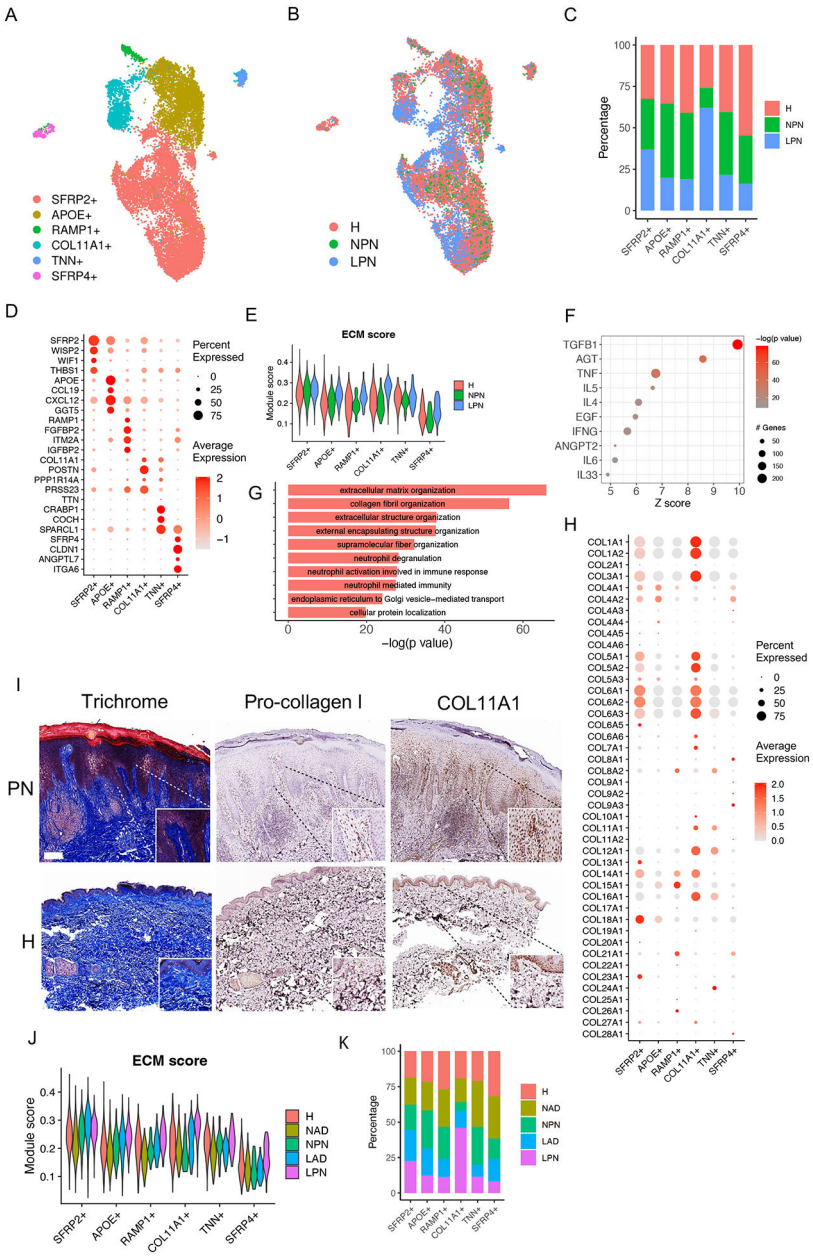

Fig.2. Identification of fibroblast subtypes.

A. UMAP showing 15,084 fibroblasts colored by subtypes.

B. UMAP plot showing the fibroblasts colored by skin conditions.

C. Bar plot showing the abundance composition across the skin conditions for each fibroblast subtype.

D. Dot plot showing the top marker genes for each fibroblast subtype. The color scale represents the scaled expression of each gene. The size of the dot represents the percentage of cells expressing the gene of interest.

E. Violin plots showing the extracellular matrix module score in the fibroblast subtypes split by the skin conditions.

F. Dot plot showing the upstream regulators for the DEGs identified in COL11A+ FB by comparing LPN to healthy cells. The color scale represents the -log10(p-value) from the enrichment analysis. The size of the dot represents the number of differentially expressed genes downstream of the upstream regulator.

G. Bar plot showing the top10 pathways enriched using the up-regulated DEGs identified in COL11A+ FB by comparing LPN to healthy cells

H. Dot plot showing the expression of all the collagen genes across the fibroblast subtypes. The color scale represents the scaled expression of each gene. The size of the dot represents the percentage of cells expressing the gene of interest.

I. Immunohistochemistry staining for Trichrome, Pro-collagen I and COL11A1 in PN and healthy tissues. The size bar indicates 100um.

J. Violin plots showing the extracellular matrix module score in the fibroblast subtypes split by the healthy, PN, and AD skin conditions.

K. The proportion of FB subtypes in healthy (H), non-lesional AD (NAD), non-lesional PN (NPN), lesional AD (LAD), and lesional PN (LPN).

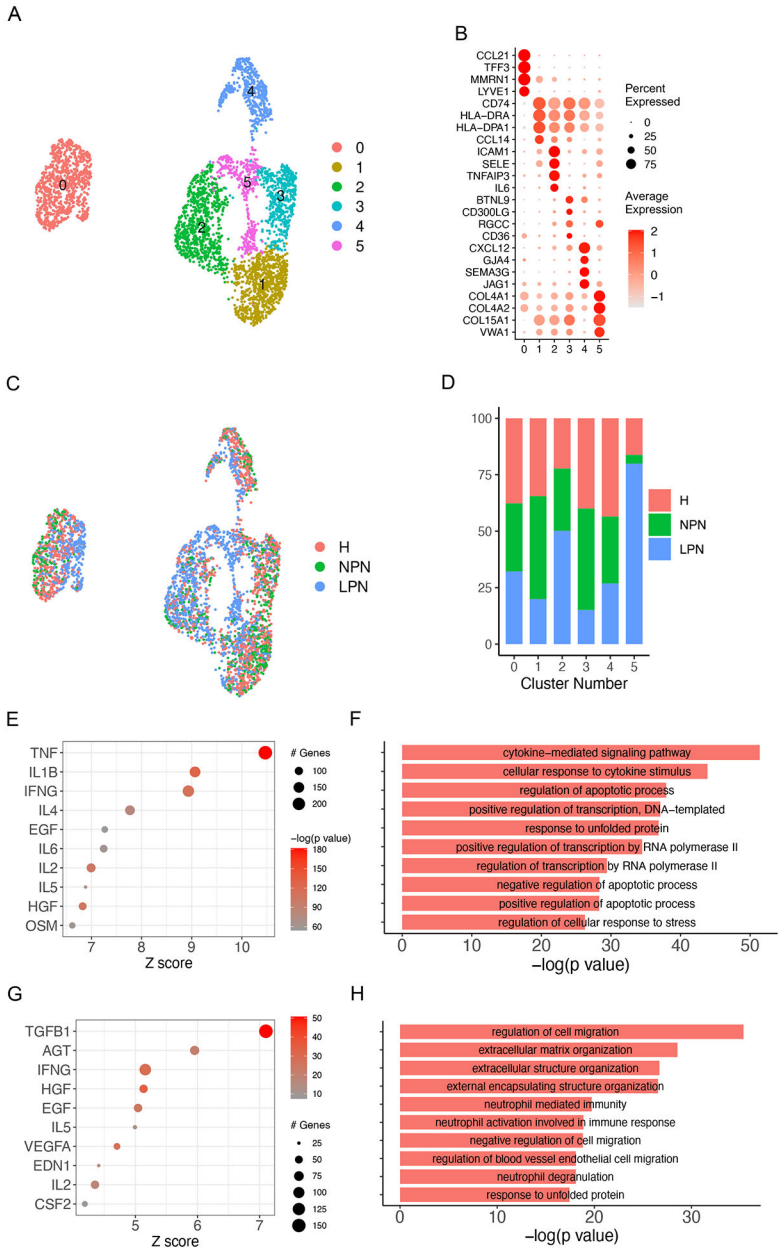

Fig.3. Identification of the endothelial subtypes.

A. UMAP plot showing 3,840 endothelial cells colored by sub-clusters.

B. Dot plot showing the top marker genes for each endothelial sub-cluster. The color scale represents the scaled expression of each gene. The size of the dot represents the percentage of cells expressing the gene of interest.

C. UMAP plot showing the endothelial cells colored by skin conditions.

D. Bar plot showing the abundance composition across the skin conditions for each endothelial sub-cluster.

E. Dot plot showing the upstream regulators for the cluster marker genes for endothelial sub-cluster 2. The color scale represents the -log10(p-value) from the enrichment analysis.

The size of the dot represents the number of differentially expressed genes downstream of the upstream regulator.

F. Bar plot showing the top10 pathways enriched using the cluster marker genes for endothelial sub-cluster 2.

G. Dot plot showing the upstream regulators for the cluster marker genes for endothelial sub-cluster 5. The color scale represents the -log10(p-value) from the enrichment analysis. The size of the dot represents the number of differentially expressed genes downstream of the upstream regulator.

H. Bar plot showing the top10 pathways enriched using the cluster marker genes for endothelial sub-cluster 5.

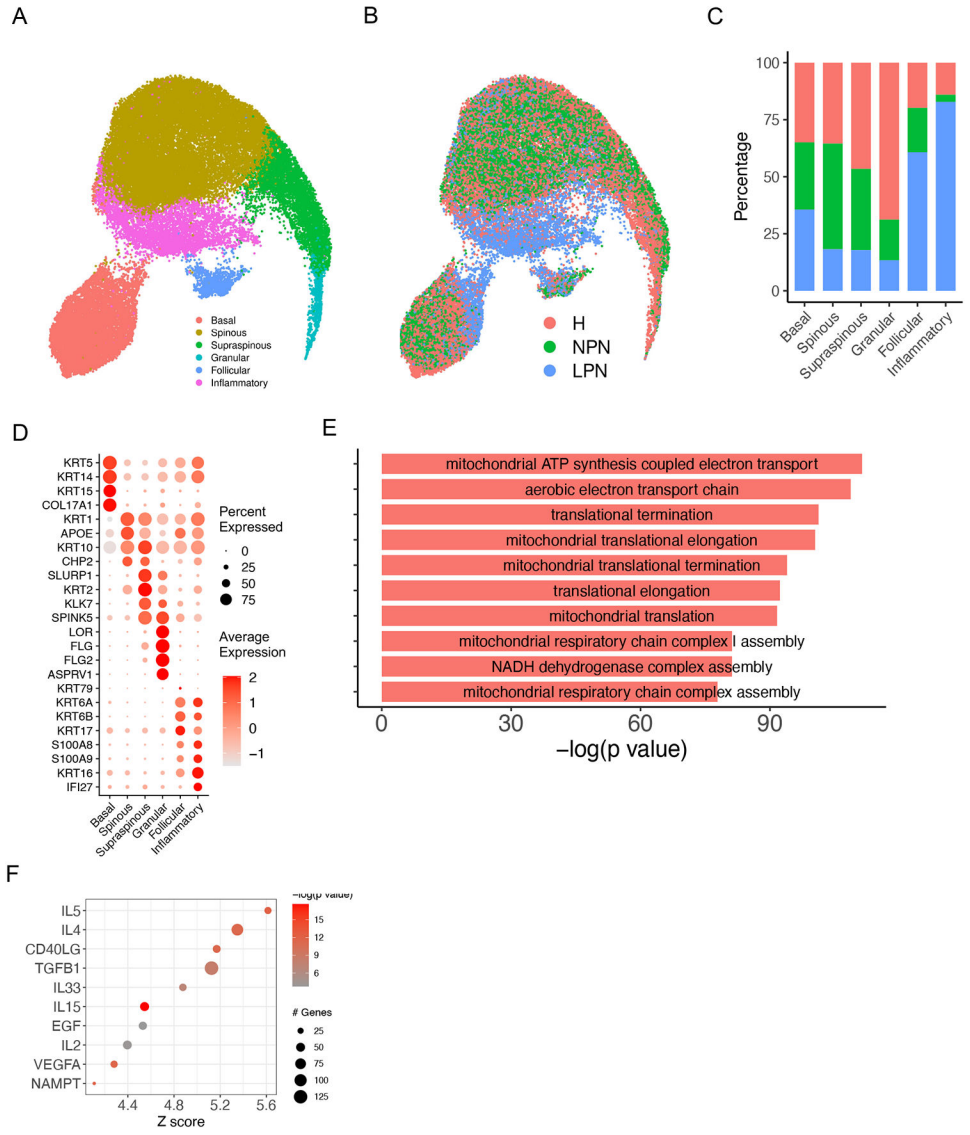

Fig. 4. Identification of the keratinocyte subtypes.

A. UMAP showing 40,277 keratinocytes colored by subtypes.

B. UMAP plot showing the keratinocytes colored by skin conditions.

C. Bar plot showing the abundance composition across the skin conditions for each keratinocyte subtype.

D. Dot plot showing the top marker genes for each keratinocyte subtype. The color scale represents the scaled expression of each gene. The size of the dot represents the percentage of cells expressing the gene of interest.

E. Bar plot showing the top 10 pathways enriched using the cluster marker genes for the inflammatory keratinocytes.

F. Dot plot showing the upstream regulators for the cluster marker genes for the inflammatory keratinocytes. The color scale represents the -log10(p-value) from the enrichment analysis. The size of the dot represents the number of differentially expressed genes downstream of the upstream regulator.

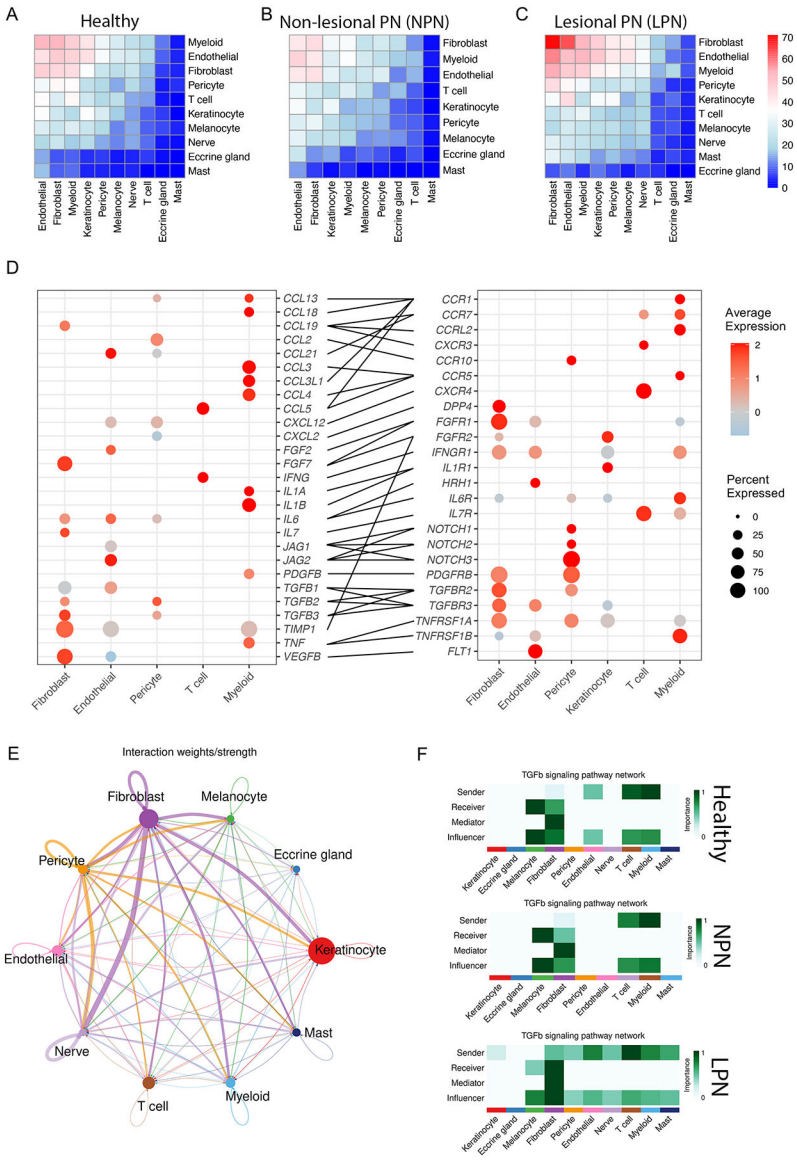

Fig 5. Cell-cell interactions revealed by ligand-receptor analysis.

A. Heatmap showing the number of ligand-receptor pairs in the healthy samples. Row, cell type expressing the ligand; column, cell type expressing the receptor. Color scale, number of ligand-receptor pairs.

B. Heatmap showing the number of ligand-receptor pairs in the NPN samples. Row, cell type expressing the ligand; column, cell type expressing the receptor. Color scale, number of ligand-receptor pairs.

C. Heatmap showing the number of ligand-receptor pairs in the LPN samples. Row, cell type expressing the ligand; column, cell type expressing the receptor. Color scale, number of ligand-receptor pairs.

D. Dot plots showing the expression of specific ligands (left) and receptors (right) that have a higher LPN interaction score than healthy samples. Color scale indicates the level of expression in the cells, whereas dot size reflects the percentage of cells expressing the gene.

E. Cell-cell interactions based on interaction weights/strengths using CellChat.
F. Heatmap of the TGFb signaling pathway network in healthy, NPN, and LPN skin outlining source (sender) and target cell (receiver, mediator, influencer). The mediator score measures a group of cells' capability as gatekeepers to control communication flow between any two cell groups. The influencer is a hybrid measure based on information centrality – a higher value indicates a greater influence on the information flow.

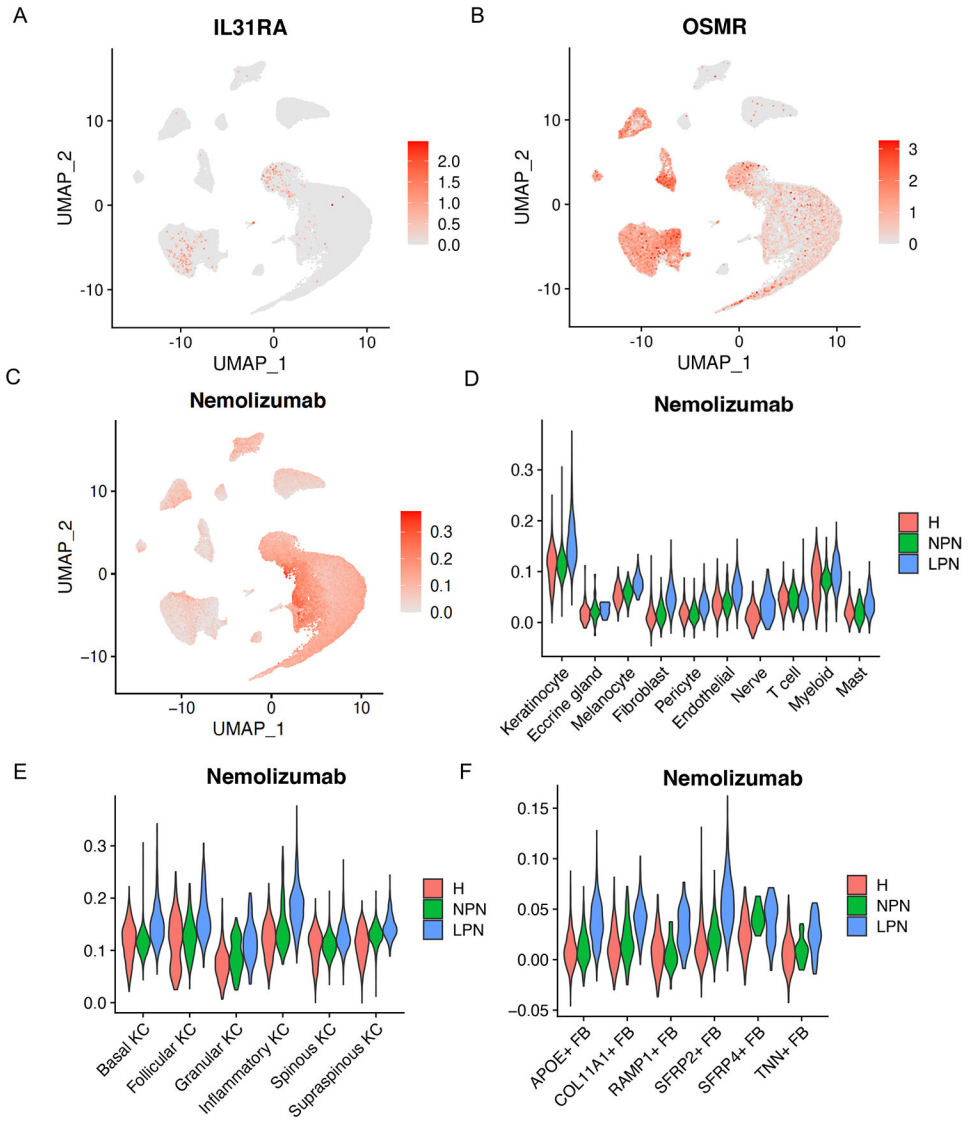

Fig. 6. Nemolizumab effects in keratinocyte and fibroblast subtypes.

A. UMAP plot showing the expression of IL31RA mainly in keratinocytes and fibroblasts.

B. UMAP plot showing the expression of OSMR mainly in keratinocytes, fibroblasts, endothelial cells, and pericytes.

C. UMAP showing overlay of DEGs decreased with nemolizumab treatment.

D. Violin plot showing the nemolizumab downregulated gene module score across major cell types in in healthy, nonlesional, and lesional PN skin.

E. Violin plot showing the nemolizumab downregulated gene module score in the keratinocyte subtypes in healthy, nonlesional, and lesional PN skin.

F. Violin plot showing the nemolizumab downregulated gene module score in the fibroblast subtypes in healthy, nonlesional, and lesional PN skin.